1994

A Zonal Method for Unsteady, Viscous, Compressible Airfoil Flows

Ekaterinaris, J.A.

Academic Press Limited

Journal of Fluids and Structures (1994) 8, 107-123
http://hdl.handle.net/10945/50280

Journal of Fluids and Structures (1994) **8**, 107–123

A ZONAL METHOD FOR UNSTEADY, VISCOUS, COMPRESSIBLE AIRFOIL FLOWS†

J. A. EKATERINARIS
Navy–NASA Joint Institute of Aeronautics, NASA Ames Research Center
Moffett Field, CA 94035, U.S.A.

AND

A. S. CRICELLI AND M. F. PLATZER
Department of Aeronautics and Astronautics, Naval Postgraduate School
Monterey, CA 93943, U.S.A.

(Received 21 October 1992 and in revised form 9 April 1993)

The analysis and prediction of fluid–structure interaction for viscous, separated flows presents a great challenge to the aeroelastician. In this paper a zonal method for the computation of unsteady, viscous, separated flows over airfoils is presented. The flowfield is divided into a viscous inner zone, where higher grid resolution may be used, and an inviscid outer zone. Zonal grid solutions are presented for subsonic and transonic flows over a NACA-0012 airfoil subject to ramp and oscillatory motions. Transonic shock/boundary layer interaction and dynamic stall effects are encountered during the unsteady motion. The computed solutions are in good agreement with available experimental data.

1. INTRODUCTION

THE ANALYSIS OF FLUID/STRUCTURE interaction problems requires efficient and accurate prediction of the airloads to which the structure is exposed. Often the flow is dominated by viscous effects involving vortices, shock waves, and large separated flow regions. In recent years, great progress has been achieved on the numerical procedures for the solution of the Reynolds averaged, Navier–Stokes equations for high-Reynolds-number two- and three-dimensional flow problems. For a review of the present state-of-the-art numerical techniques we refer to the text by Hirsch (1990), the recent review paper by Hänel (1992) and the references listed therein.

Navier–Stokes methods require computational meshes with sufficient grid clustering near the wall for the accurate prediction of the large flow gradients in the viscous layers. The mesh outer boundaries must be placed far enough, in order to apply the inflow/outflow boundary conditions. However, only a coarser grid is required for the computation in the flow regions where viscous effects are not significant and the flow gradients are small.

Accurate prediction of turbulent high Reynolds number flow poses a great challenge to the computational fluid dynamicist. An additional challenge is encountered in transonic flows due to the occurrence of weak shocks and shock/boundary layer interactions. For example, recent experimental investigations of unsteady flows over

† Originally presented at the 30th Aerospace Sciences Meeting and Exhibit, 6–9 January 1992, Reno, Nevada, U.S.A.

0889–9746/94/010107 + 17 $08.00

pitching and oscillating airfoils by Chandrasekhara *et al.* (1990) have shown that at free-stream Mach numbers greater than 0·4, shocks are generated near the airfoil leading edge. The computation of these shocks requires the use of sufficient grid resolution and high-order accurate shock capturing schemes. Recent developments of high-order upwind shock capturing schemes (Roe 1985; Rai 1986; Rai & Chakravarthy 1986) enable accurate capturing of flow discontinuities for a variety of flow regimes. Solutions obtained for two and three-dimensional complex flow fields by Rai (1987a, b) have proven the accuracy of upwind methods.

Unsteady solutions for pitching and oscillating airfoils have been computed in the past by Rumsey & Anderson (1988), Visbal (1988) and Ekaterinaris (1989) using a single grid approach. The need for a decomposition of the flow domain into subdomains in order to enable gridding of complex flow domains and to meet conflicting requirements of accuracy versus efficiency has been recognized by several researchers. The Chimera approach pioneered by Benek *et al.* (1985) is the most general one which has been implemented to date. This approach requires significant bookkeeping in order to find the relative location of the overlapped grids and to obtain the weights for the intepolation which establishes the communication between the grids. Rai (1986) developed a conservative scheme for boundary information transfer between patched grids. Recently, a zonal approach has been also reported by Chesshire & Hershaw (1990).

In the present paper, a zonal method for the computation of unsteady, compressible, viscous flows is presented. This approach, in contrast to the Chimera approach, does not require bookkeeping, and yet enables unsteady solutions on moving fine grids close to the airfoil surface for capturing of the viscous flow effects, in combination with a coarser grid for the outer inviscid flow. The Osher (1982, 1983) upwind scheme in its implicit form presented by Rai & Chakravarthy (1986) is implemented to evaluate the inviscid fluxes. The implicit part of the algorithm is approximately factorized and linearized, and the solution is obtained with an iterative time-marching scheme. The physical domain is decomposed into two zones. The inner zone consists of an O-type mesh which surrounds the airfoil. The outer boundary of the inner grid is circular. The outer zone starts from the outermost circle of the inner grid and extends to the far field or to a specified flow boundary. The inner and outer grids overlap by three points at the circumferential grid lines. Because of the circular interface, the inner and outer grid circumferential lines never intersect even when the inner grid is rotated. In this manner, the two grids are generated independently and different computational techniques may be applied for the solution in each zone, if needed.

At the zonal grid interfaces boundary-information transfer is significantly facilitated, because the grid boundaries coincide along the circumferential direction. At the overlapped interfaces, boundary information transfer is obtained by simple weighted averaging. Computation of the relative locations of the two grids and the weights of the interpolation is simple and computationally inexpensive. A simple zonal grid, where the inner and outer grids overlap by three points, is shown in Figure 1.

At the zonal interface, the conservative variables are transferred from one grid to the other. This approach is not fully conservative, in contrast to the approach employed by Rai (1986) for patched grids, where the fluxes, instead of the flow variables, are transferred in a fully conservative manner. However, transfer of the conservative variables provides the flexibility of applying different solution techniques for the inner and outer grids, and overlapping allows to retain accuracy at the zonal interface. Solutions obtained for transonic flows, with zonal interfaces close to the airfoil, show that shocks can pass through the zonal interface without distortion.

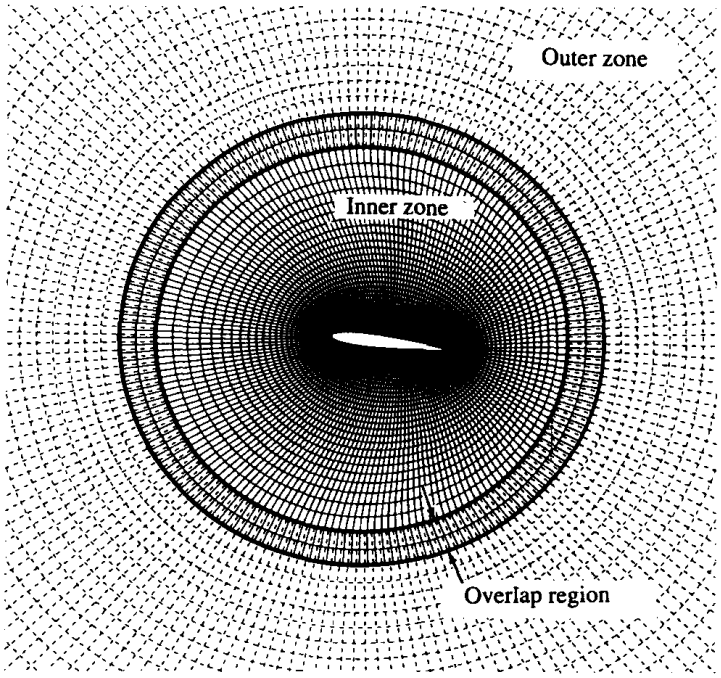

Figure 1. Sample zonal grid over a NACA-0012 airfoil.

Steady inviscid and viscous solutions for different circumferential resolution of the inner and outer grids are obtained, and the results are compared with available experimental data. For the viscous computations, only the inner grid solution includes the viscous terms, while the outer grid region is considered inviscid. Unsteady solutions over oscillating and rapidly pitching airfoils are obtained by rotating the inner grid.

2. NUMERICAL METHOD

2.1. Governing Equations

The strong conservation-law form of the governing Euler and thin-layer, compressible Navier–Stokes equations for a curvilinear coordinate system (ξ, ζ) along the axial and normal direction, respectively, is as follows

$$\partial_t \hat{\boldsymbol{Q}} + \partial_\xi \hat{\boldsymbol{F}} + \partial_\zeta \hat{\boldsymbol{G}} = \mathrm{Re}^{-1} \partial_\zeta \hat{\boldsymbol{S}}. \tag{1}$$

The Euler equations are obtained when the right-hand side is set equal to zero. In equation (1), $\hat{\boldsymbol{Q}}$ is the conservative variable vector, $\hat{\boldsymbol{F}}$ and $\hat{\boldsymbol{G}}$ are the inviscid flux vectors, and $\hat{\boldsymbol{S}}$ represents the viscous terms in the normal direction. The conservative variable vector $\hat{\boldsymbol{Q}}$ is

$$\hat{\boldsymbol{Q}} = \frac{1}{J} \begin{Bmatrix} \rho \\ \rho u \\ \rho w \\ e \end{Bmatrix},$$

where $J = 1/(x_\xi z_\zeta - x_\zeta z_\xi) = \xi_x \zeta_z - \xi_z \zeta_x$ is the Jacobian of the transformation. $\hat{\boldsymbol{F}}$ and $\hat{\boldsymbol{G}}$ are the invisid fluxes given by

$$\hat{\boldsymbol{F}} = \frac{1}{J} \begin{Bmatrix} \rho U \\ \rho u U + \xi_x p \\ \rho w U + \xi_z p \\ (e+p)U - \xi_t p \end{Bmatrix}, \qquad \hat{\boldsymbol{G}} = \frac{1}{J} \begin{Bmatrix} \rho W \\ \rho u W + \zeta_x p \\ \rho w W + \zeta_z p \\ (e+p)W - \zeta_t p \end{Bmatrix}.$$

The viscous term, when the thin-layer approximation is applied, and assuming that $\lambda = -2/3\mu$ is given by

$$\hat{\boldsymbol{S}} = \frac{1}{J}\begin{Bmatrix} 0 \\ \mu m_1 u_\zeta + (\mu/3) m_2 \zeta_x \\ \mu m_1 w_\zeta + (\mu/3) m_2 \zeta_z \\ \mu m_1 m_3 + (\mu/3) m_2^+ m_4 \end{Bmatrix},$$

where

$$m_1 = \zeta_x^2 + \zeta_z^2, \qquad m_2 = \zeta_x u_\zeta + \zeta_z w_\zeta,$$
$$m_3 = \frac{\partial}{\partial \zeta}(u^2 + w^2)/2 + \kappa \,\mathrm{Pr}^{-1}\left(\frac{\partial a^2}{\partial \zeta}\right), \qquad m_4 = (\zeta_x u + \zeta_z w);$$

a is the local speed of sound, κ is the thermal conductivity, Pr is the Prandtl number, and U, W are the contravariant velocity components given by

$$U = u\xi_x + w\xi_z + \xi_t, \qquad W = u\zeta_x + w\zeta_z + \zeta_t.$$

In equation (1), all geometrical dimensions are normalized with the airfoil root-chord length; the density is normalized with the free-stream density, ρ_∞; the velocity components are normalized with the free-stream speed of sound, a_∞; the total energy per unit volume is normalized with $\rho_\infty a_\infty^2$; and the pressure is related to density and total energy through the equation of state for an ideal gas, $p = (\gamma - 1)[e - \frac{1}{2}\rho(u^2 + w^2)]$.

2.2. Numerical Implementation

The numerical integration is performed using an upwind-biased, factorized, iterative, implicity numerical scheme given by

$$\begin{aligned}
&[I + h_\xi(\nabla_\xi^b \tilde{A}_{i,k}^+ + \Delta_\xi^f \tilde{A}_{i,k}^-)]^p \\
&\quad \times [I + h_\zeta(\nabla_\zeta^b \tilde{B}_{i,k}^+ + \Delta_\zeta^f \tilde{B}_{i,k}^- - \mathrm{Re}^{-1}\,\delta_\zeta \tilde{M}_{i,k})]^p \times (\tilde{Q}_{i,k}^{p+1} - \tilde{Q}_{i,k}^p) \\
&\quad = -[(\tilde{Q}_{i,k}^p - Q_{i,k}^n) + h_\xi(\hat{F}_{i+1/2,k}^p - \hat{F}_{i-1/2,k}^p) + h_\zeta(\hat{G}_{i,k+1/2}^p - \hat{G}_{i,k-1/2}^p) \\
&\quad\quad - \mathrm{Re}^{-1} h_\zeta(\hat{S}_{i,k+1/2}^p - \hat{S}_{i,k-1/2}^p)]
\end{aligned} \tag{2}$$

where $h_\xi = \Delta\tau/\Delta\xi$, etc., $\tilde{A}^\pm = (\partial\tilde{F}/\partial\tilde{Q})$, etc., are the flux Jacobian matrices, and Δ, ∇, and δ are the forward, backward and central difference operators, respectively. The quantities $\tilde{F}_{i+1/2,k}$, $\tilde{G}_{i,k+1/2}$, and $\tilde{S}_{i,k+1/2}$ are numerical fluxes.

Time accuracy of the implicit numerical solution is obtained by performing Newton iteration to convergence within each time step. The approximation to $\tilde{Q}^{n+1}$ at each subiteration is the quantity $\tilde{Q}^p$. When $p \geq 2$, during a given subiteration, $\tilde{Q}^p = \tilde{Q}^{n+1}$, but when $p = 1$ and no subiterations are performed, then $\tilde{Q}^p = \tilde{Q}^n$, and $\tilde{Q}^{p+1} = \tilde{Q}^{n+1}$. By subiterating to convergence, linearization and factorization errors are minimized, because the left-hand side of equation (2) can be driven to zero at each time step. The inviscid fluxes $\hat{F}$ and $\hat{G}$ are evaluated using Osher's (1982, 1983) upwinding scheme.

The numerical fluxes for a third-order accurate upwind-biased scheme are given by

$$\begin{aligned}
\hat{F}_{i+1/2,k} &= \tilde{F}_{i+1/2,k} + \tfrac{1}{6}[\Delta F_{i-1/2,k}^+ + 2\Delta F_{1+1/2,k}^+] \\
&\quad - \tfrac{1}{6}[\Delta F_{i+3/2,k}^- + 2\Delta F_{1+1/2,k}^-] \\
&= \tilde{F}(Q_{i,k}, Q_{i+1,k}) + \tfrac{1}{6}[\Delta F^+(Q_{i+1,k}, Q_{i,k}) + 2\Delta F^+(Q_{i,k}, Q_{i+1,k})] \\
&\quad - \tfrac{1}{6}[\Delta F^-(Q_{i,k}, Q_{i+1,k}) + 2\Delta F^-(Q_{i+1,k}, Q_{i,k})];
\end{aligned} \tag{3}$$

here $\tilde{F}$ is the first-order accurate numerical flux for the Osher's (1982, 1983) scheme given by

$$\tilde{F}_{i+1/2,k} = \frac{1}{2}\left[F_{i,k} + F_{i+1,k} - \int_{Q_i}^{Q_{i+1}} \{F_q^+ - F_q^-\}\, dQ\right], \tag{4}$$

where $F_q = F_q^+ + F_q^-$, $F_q^\pm = (\partial F/\partial Q)^\pm$, and $\Delta F^\pm$ are the corrections to obtain high-order accuracy. The Osher scheme evaluates the flux assuming a shock-tube solution where F_q is piecewise continuous, and yields good predictions of the flux, especially at supersonic Mach numbers. For the linearization of the left-hand side of equation (2), the flux Jacobian matrices A, B are evaluated by the Steger–Warming (1981) flux-vector splitting. The linearization errors are reduced by subiteration to convergence. Typically, two to three subiterations are sufficient to drop the residuals two orders of magnitude during the Newton iteration process. Accurate steady-state solutions can be obtained even without subiteration. Two subiterations are used for the unsteady solutions.

High-order accurate shock-capturing schemes have some limitations; they may select a nonphysical solution, such as expansion shocks violating the entropy condition as explained by Osher *et al.* (1982, 1983) and Hirsch (1990); they may produce spurious oscillations and they may develop nonlinear instability in nonsmooth and discontinuous flow regions. More appropriate high-order shock-capturing schemes suitable for the computation of flows with shocks are the TVD schemes, described in detail by Yee *et al.* (1983) and Yee (1989).

In the present study, the Osher–Chakravarthy TVD scheme (Chakravarthy & Osher 1985), is used. This TVD scheme has flux limiters which impose constraints on the gradients of the fluxes. The flux-limited values $\Delta\tilde{f}^\pm$ are computed from the unlimited fluxes $\Delta f^\pm$ as follows:

$$\begin{aligned}
\Delta\tilde{f}^-_{i+3/2,k} &= \text{minmod}[\Delta f^-_{i+3/2,k},\ \beta\, \Delta f^-_{i+1/2,k}],\\
\Delta\tilde{f}^-_{i+1/2,k} &= \text{minmod}[\Delta f^-_{i+1/2,k},\ \beta\, \Delta g^-_{i+3/2,k}],\\
\Delta\tilde{f}^+_{i+1/2,k} &= \text{minmod}[\Delta f^+_{i+1/2,k},\ \beta\, \Delta f^+_{i-1/2,k}],\\
\Delta\tilde{f}^+_{i-1/2,k} &= \text{minmod}[\Delta f^+_{i-1/2,k},\ \beta\, \Delta f^+_{i+1/2,k}],
\end{aligned} \tag{5}$$

where the minmod operator is defined by

$$\text{minmod}[x, y] = \text{sign}(x) \times \max[0, \min\{|x|, y\ \text{sign}(x)\}]. \tag{6}$$

The viscous fluxes $S_{i,k+1/2}$ are computed with central differences as follows:

$$\begin{aligned}
S_{i,k+1/2} &= S[Q_{i,k+1/2},\ (Q_\zeta)_{i,k+1/2},\ \zeta_{i,k+1/2}],\\
Q_{i,k+1/2} &= \tfrac{1}{2}(Q_{i,k} + Q_{i+1,k}), \qquad (Q_\zeta)_{i,k+1/2} = Q_{i,k+1} - Q_{i,k}.
\end{aligned} \tag{7}$$

The experimental Reynolds numbers based on the chord length for the test cases examined are in the range $3{\cdot}0 \times 10^6 \le \text{Re}_c \le 5{\cdot}0 \times 10^6$, and it is expected that the flow is mostly turbulent. Transitional flow is expected to have an effect at regions very close to the leading edge. As shown by Jang *et al.* (1991), the incorporation of transition modelling is essential for the successful prediction of separation bubbles on airfoils at chord Reynolds numbers less than one million. However, in this paper high Reynolds number flows only are considered. In the present work, the widely used two-layer Baldwin–Lomax (1978) turbulence model is used. The effectiveness of other turbulence models, such as the Johnson–King model (Johnson & King 1985) and the RNG based algebraic model developed by Yakhot & Orszag (1986) for steady and unsteady flows, were investigated by Clarkson *et al.* (1993). The conclusion of that study was that for mildly separated flows, such as the light stall cases considered here, the effect of the turbulence model on the prediction of the aerodynamic loads is not very significant.

3. BOUNDARY CONDITIONS

The solutions on the two grids are computed separately, with the inner and outer solutions communicating through the zonal interface boundary. The inner grid surrounds the airfoil and includes the boundary layer region and the wake for viscous solutions. Inviscid solutions are obtained by applying the nonpenetration slip condition, where the normal contravariant velocity component, W, is set equal to zero on the surface. For viscous solutions, the nonslip condition is applied for the velocities on the airfoil surface. In both cases, the density and the pressure are obtained from the interior by simple extrapolation. For unsteady solutions, the surface velocity is set equal to the airfoil speed obtained by the prescribed airfoil motion as follows:

$$u = \frac{1}{J}(\zeta_t \xi_z - \xi_t \zeta_z), \qquad w = \frac{1}{J}(\xi_t \zeta_x - \zeta_t \xi_x). \tag{8}$$

Unsteady solutions for pitching and oscillating airfoils are obtained by rotating the inner grid only. The inner grid is rotated without deformation, as a solid body. The unsteady motion may also be obtained by shearing the grid, but this approach produces severely skewed grids for large rotations. For the unsteady solutions only the metrics of the inner grid must be recomputed at each time step.

At the inner zonal interface, the flow variables are obtained from the interior of the outer grid solution. Similarly, the inner zonal boundary of the outer grid obtains boundary information from the interior of the inner grid. The inner and outer grid radial lines (Figure 1) are not aligned, in general. The relative location of the two grids with respect to the inertial reference frame varies during the motion of the inner grid. The distances between neighboring points at the zonal interface are computed, and simple weighted averaging of the conservative variables is applied.

All flows were computed for subsonic free-stream speeds. For subsonic inflow/outflow boundaries of the outer grid, the flow variables are evaluated using one dimensional Riemann invariant extrapolation. At the inflow boundary there are three incoming and one outgoing characteristics. Therefore, three primitive variables are specified: the density ρ, the normal velocity w, and the pressure p; the fourth variable, the axial velocity u, is extrapolated from the interior. The inflow boundary conditions are given by

$$\begin{gathered} \rho_1 = \left(\frac{a_1^2}{\gamma s_1}\right)^{(1/\gamma - 1)}, \qquad s_1 = \left(\frac{p_\infty}{\rho_\infty^\gamma}\right), \qquad a_1 = \frac{(\gamma - 1)}{4}(R_1^+ - R_2^-) \\ u_1 = \tfrac{1}{2}(R_1^+ + R_2^-), \qquad w_1 = w_\infty, \qquad p_1 = \left(\frac{\rho_1 a_1^2}{\gamma}\right), \end{gathered} \tag{9}$$

where R_1^+ and R_2^- are the incoming and outgoing Riemann invariants given by

$$R_1^+ = u_\infty + 2a_\infty/(\gamma - 1), \qquad R_2^- = u_2 - 2a_2/(\gamma - 1).$$

At the outflow boundary there are one incoming and three outgoing characteristics. Therefore, only one quantity, the pressure, is specified, while the others are extrapolated from the interior. For the density and normal velocity, simple first-order extrapolation is used, and the axial outflow velocity is obtained from the zero-order outgoing Riemann invariant. The outflow boundary conditions are given by

$$\begin{gathered} \rho_1 = \rho_2, \qquad u_1 = R_1^+ - 2a_1/(\gamma - 1), \\ a_1 = \sqrt{\gamma p_1/\rho_1}, \qquad w_1 = w_2, \qquad p_1 = p_\infty. \end{gathered} \tag{10}$$

For the viscous flow solutions the viscous terms were included only for the inner grid. For the outer grid, where the viscous effects are small, the inviscid flow equations were solved. For the unsteady flow solutions, the outer grid remained stationary and the metrics were not re-evaluated at each time step.

4. RESULTS AND DISCUSSION

The validity of the zonal grid approach is first demonstrated for inviscid solutions. The main objective is to assess the accuracy and the conservative character of the solution for different locations of the zonal interface and grid densities. An advantage of the present approach is that different grid densities may be used for the inner and outer grids.

The accuracy of the computed results for different inner and outer grid densities is tested. The effect of the location of the zonal interface relative to the airfoil on the accuracy of the solution is also investigated. Several viscous solutions at fixed angles of incidence, up to approximately the static stall angle, are computed. Finally, unsteady flow responses to a ramp motion at subsonic free-stream speed of $M_\infty = 0{\cdot}3$ and for oscillation at a free-stream speed of $M_\infty = 0{\cdot}6$ are also computed.

5. STEADY-STATE SOLUTIONS

The accuracy of the present method was first established by computing steady-state inviscid and viscous solutions for a variety of flow conditions and angles of incidence. The computed results are compared with the experimental measurements of Harris (1981) and, when possible, to a panel solution.

5.1. Inviscid Solutions

A two-block grid consisting of an 81×21 point O-type inner grid and an 81×21 point outer grid was used as baseline grid for the inviscid solutions. An inviscid solution using the baseline grid for subsonic flow over a NACA-0012 airfoil at $M_\infty = 0{\cdot}7$, $\alpha = 1{\cdot}4°$ was obtained. The computed surface-pressure coefficient distribution is compared with the measurements of Harris (1981) in Figure 2. The agreement with the experiment is satisfactory. The ability of the zonal scheme to treat flow discontinuities was investigated for a transonic flow solution at $M_\infty = 0{\cdot}803$, $\alpha = -0{\cdot}1°$. The surface-pressure coefficient distribution predicted from the inviscid solution using the baseline

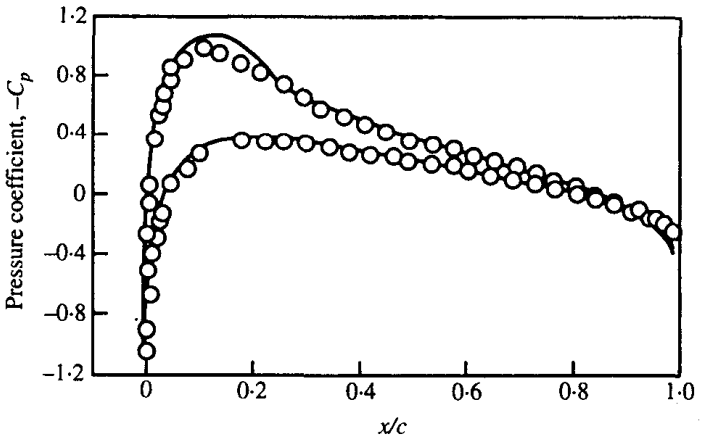

Figure 2. Comparison of the computed and measured surface-pressure coefficient for an inviscid, shock-free solution; $M_\infty = 0{\cdot}7$, $\alpha = 1{\cdot}4°$, O, Measured (*Harris* 1981); ——, computed.

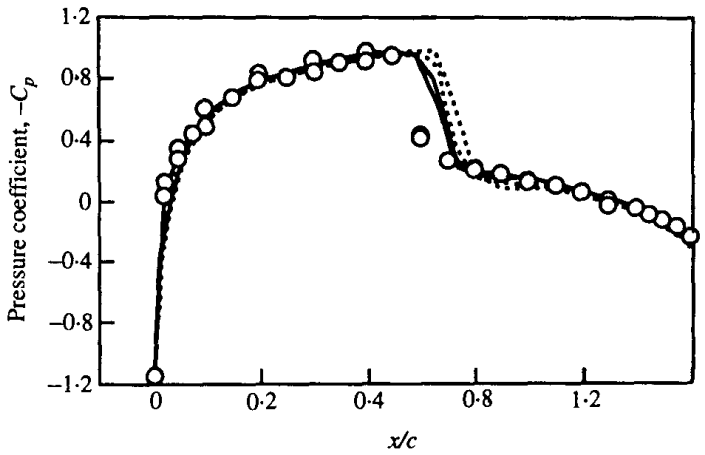

Figure 3. Effect of grid density on the prediction of pressure coefficient for an *inviscid* transonic flow; $M_\infty = 0{\cdot}8$, $\alpha = -0{\cdot}1°$. ○, Measured (Harris 1981); ——, computed (baseline grid); - - -, computed (half resolution).

grid is compared with the measurements of Harris (1981) in Figure 3. The shock is captured within two points with the baseline grid solution. The effect of the grid resolution on the prediction of the surface pressure coefficient is shown in the same figure. Solutions were obtained with half the streamwise resolution, e.g., a 41×21 point grid. The surface-pressure coefficient distribution obtained from this solution (Figure 3) is in general agreement with the baseline grid predictions, but it predicts the shock location further downstream due to lack of streamwise resolution. The predictions with an even coarser grid, e.g., a 41×11 point grid, predicted the shock location even further downstream.

The solution on a zonal grid where the outer boundary of the inner grid was placed close enough to the airfoil so that the shock would cross the zonal interface was also obtained. Note that, for this case, an oval type of zonal interface was used, because the available grid-generation procedure was incapable of constructing an inner grid with a circular outer boundary placed close enough to the airfoil. The computed surface-pressure coefficient distribution (not shown here) was in perfect agreement with the predictions shown in Figure 3. The computed flow quantities, such as density and pressure, showed that the zonal approach used can pass shocks through the zonal interface. In Figure 4 the computed Mach contours are shown, the shock location is indicated with the sonic line, and the zonal interface is indicated with a dashed line. The Mach contour lines cross the zonal boundary without distortion, and the shock is convected through the zonal interface. The preliminary test cases presented above were computed on regularly stretched inner/outer grids.

5.2. Viscous Flow Solutions

Viscous, subsonic flow solutions were obtained at several fixed angles of attack. The flow conditions of the measurements reported by Harris (1981) were used, e.g., $M_\infty = 0{\cdot}3$, $Re = 4{\cdot}0 \times 10^6$. These solutions were obtained on a 181×56 point viscous inner grid and a 181×26 point inviscid outer grid. Solutions were also computed on a grid with half the streamwise resolution, e.g., a 91×56 point grid.

The computed surface pressure coefficient distributions for several angles of incidence are compared in Figure 5. In the same figure, the predictions of the inviscid, incompressible panel method of Jang *et al.* (1991) are also shown. Solutions for fixed angles of incidence were obtained by either rotating the inner grid to the specified

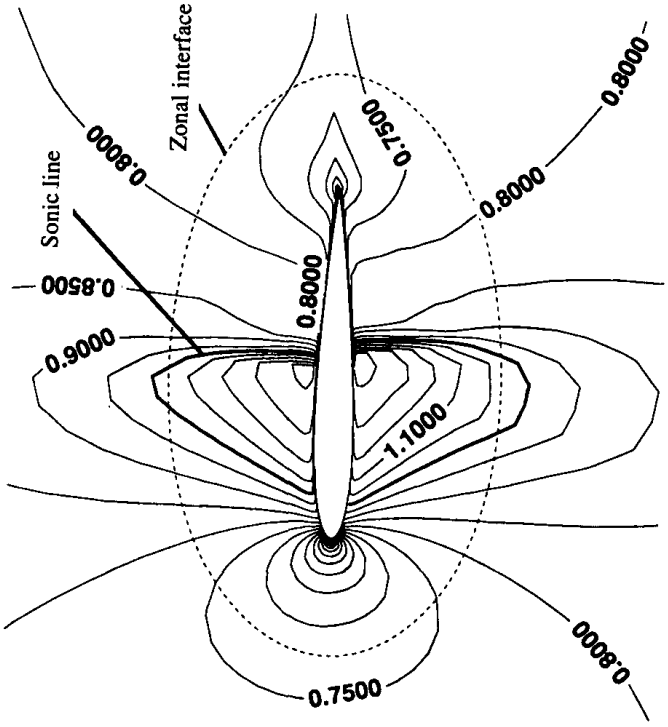

Figure 4. Computed Mach contours; $M_\infty = 0{\cdot}8$, $\alpha = 0{\cdot}1°$, inviscid calculations.

angle of incidence and setting the oncoming flow to zero degrees or by not rotating the inner grid and setting the oncoming flow to the specific angle of incidence. Both approaches were straightforward to implement and the computed results were in both cases the same. For the subsonic viscous solutions, no flux limiting was applied.

6. UNSTEADY SOLUTIONS

6.1. Ramp Motion

The unsteady solution for a ramp motion from $\alpha = 0$ to $\alpha = 15{\cdot}5°$ at $M_\infty = 0{\cdot}3$, $Re = 2{\cdot}7 \times 10^6$ and pitch rate $k = 0{\cdot}0127$ was obtained on both a 91×56 point inner grid and a 181×56 point inner grid. The pitch rate is defined as $k = \dot{\alpha}c/2U_\infty$.

The computed lift response is compared with the experimental measurements by Landon (1982) in Figure 6. Both the coarse and the fine grid solutions closely predict the measured lift. However, at the higher angles of attack, the finer grid gives higher lift. The surface-pressure coefficient distributions at several angles of incidence are compared in Figure 7. The computed surface-pressure coefficient distribution is in good agreement with the measured data over the entire incidence range.

The computed boundary-layer profiles at a midchord point for $\alpha = 5{\cdot}8°$, $8{\cdot}9°$, $11{\cdot}7$, and $15{\cdot}5°$ are compared in Figure 8 with the predictions of a boundary-layer computation of Jang *et al.* (1991) based on an unsteady viscous-inviscid interaction method. The solutions have been computed with different grid densities (approximately triple of the Navier–Stokes grid resolution in the normal direction is used for the boundary-layer solution). Also, the Cebeci–Smith turbulence model has been used for the boundary-layer solution. The computed velocity profiles predicted by the two methods are in very good agreement for all angles of incidence before the flow separates. At $\alpha = 15{\cdot}5°$, both solutions predicted flow reversal at the trailing edge only.

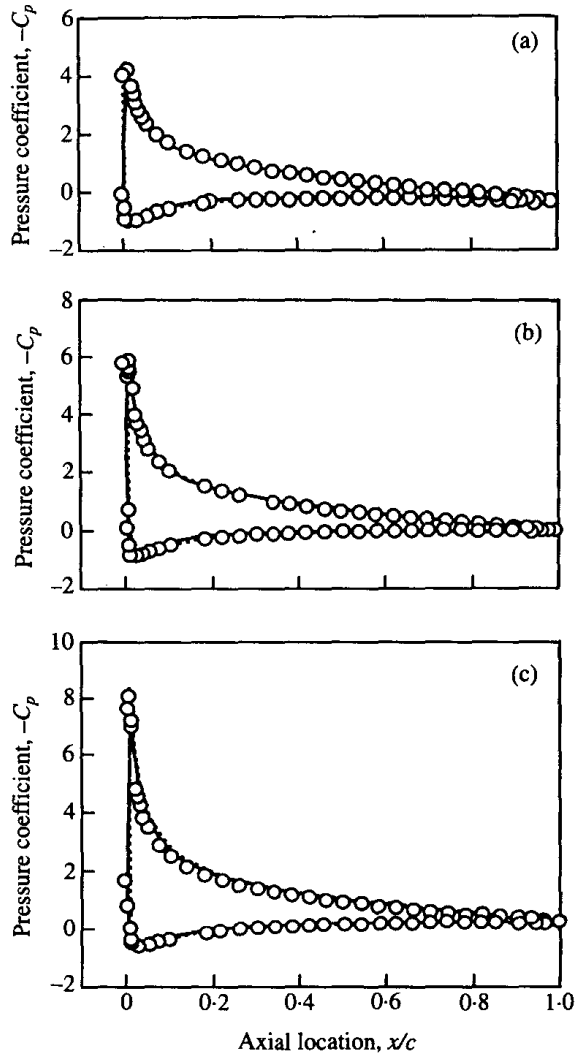

Figure 5. Comparison of the measured and computed pressure coefficient for (a) $\alpha = 8{\cdot}3°$, (b) $\alpha = 10{\cdot}1°$, and (c) $\alpha = 11{\cdot}9°$; $M_\infty = 0{\cdot}3$, $Re = 4{\cdot}0 \times 10^6$, turbulent. ○, Measured (Harris 1981); ——, computed (181×56 grid); - - -, computed (inviscid panel method).

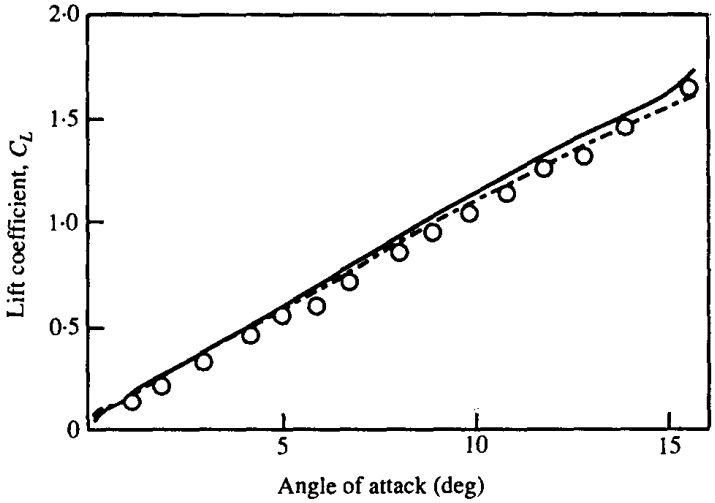

Figure 6. Comparison of the measured and computed lift coefficient for a ramp motion from $\alpha = 0°$ to $\alpha = 15{\cdot}5°$ with pitch rate $k = 0{\cdot}0127$; $M_\infty = 0{\cdot}3$, $Re = 2{\cdot}7 \times 10^6$, turbulent. ○, Measured (Landon 1982); ——, computed (181×56 grid); – – –, computed (91×56 grid).

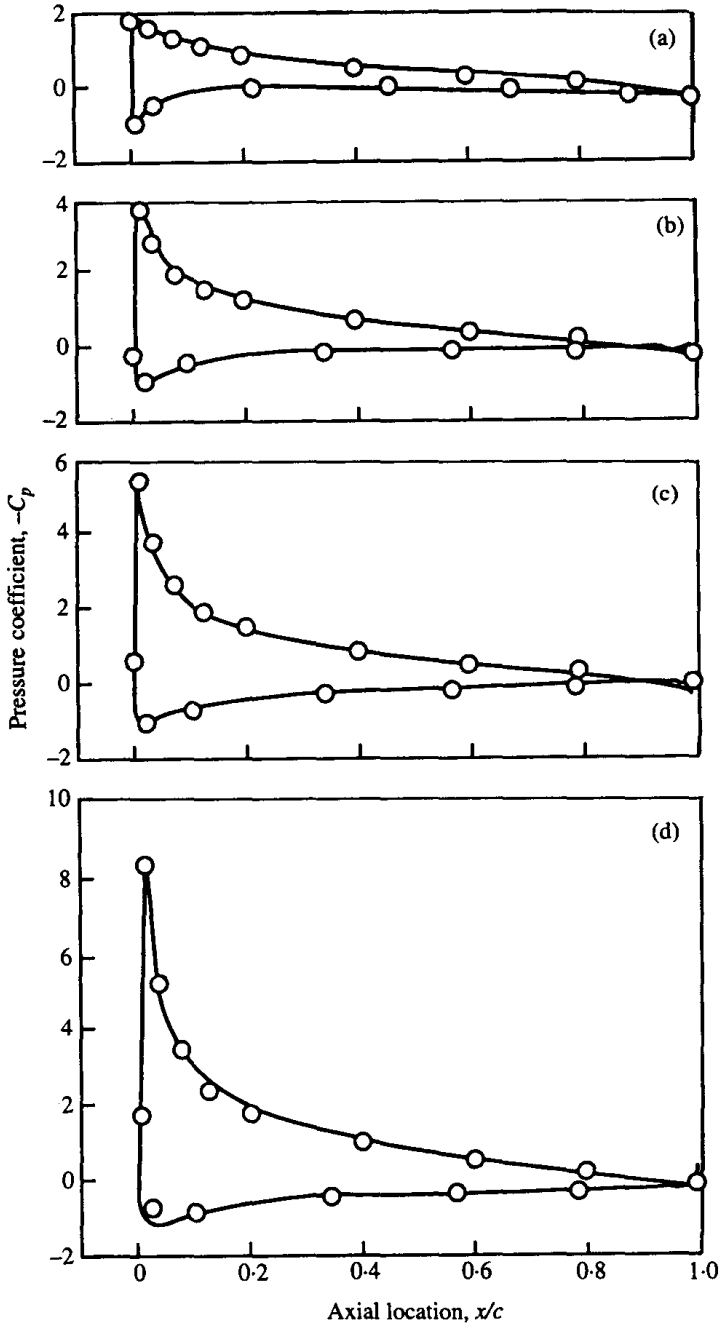

Figure 7. Comparison of measured and computed unsteady surface pressure coefficient for (a) $\alpha = 5{\cdot}8°$, (b) $\alpha = 8{\cdot}9°$, (c) $\alpha = 11{\cdot}7°$, and (d) $\alpha = 15{\cdot}5°$; $M_\infty = 0{\cdot}3$, $Re = 2{\cdot}7 \times 10^6$, turbulent. ○, Measured (Landon 1982); ——, computed (181 × 56 grid).

The computed results are in close agreement in the near wall region. The grid resolution for the Navier–Stokes solution at this angle of incidence is sufficient, and y^+ is of the order of one. It is concluded, therefore, that the differences observed in the outer wall region are mainly due to the different turbulence models.

The computed flowfield at the maximum angle of incidence for which experimental data are available, $\alpha = 15{\cdot}5°$, is mostly attached. A small separated flow region exists at the trailing edge region only. Unsteady solutions at a higher angle of attack, $\alpha \approx 17{\cdot}0°$, show development of the dynamic stall vortex at the leading edge region. The computed flowfield at $\alpha = 15{\cdot}5°$ is shown in Figure 9(a–c). Figure 9(a) shows a global

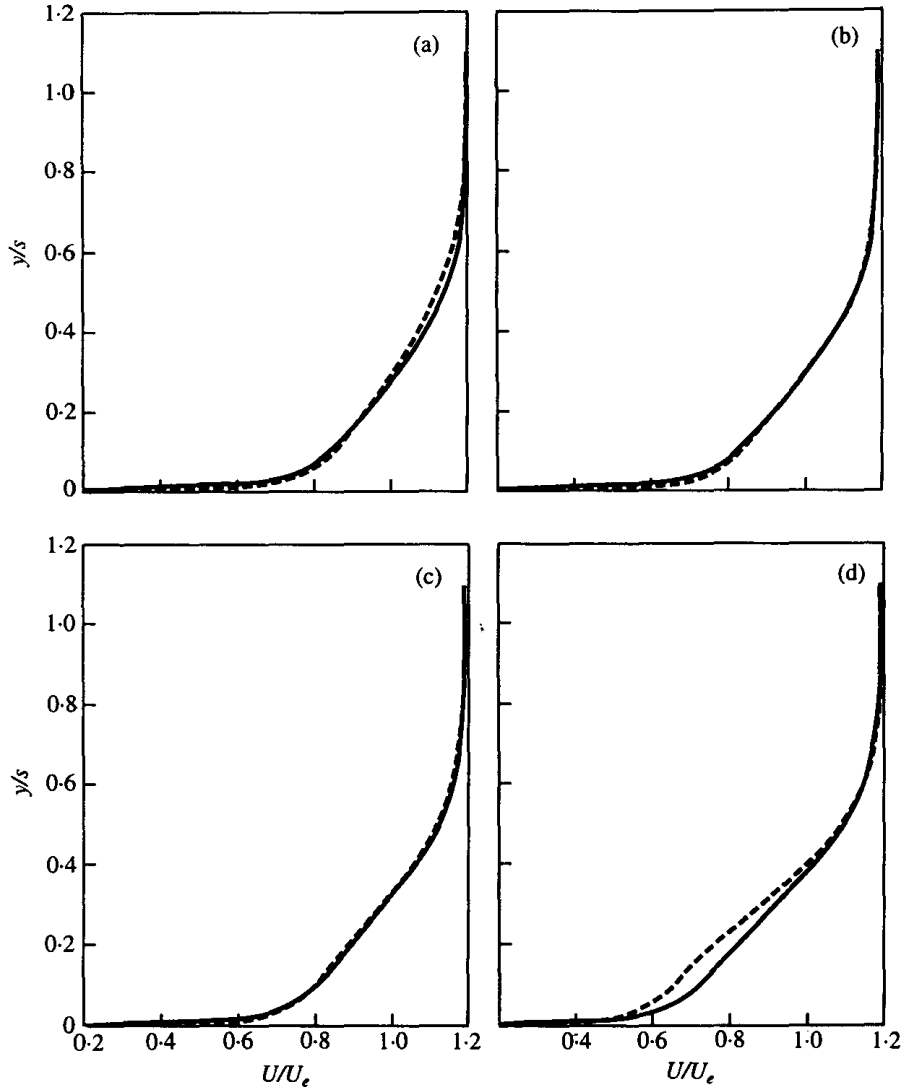

Figure 8. Comparison of the computed unsteady velocity profiles for $\alpha = 5{\cdot}8°$, (b) $\alpha = 8{\cdot}9°$, (c) $\alpha = 11{\cdot}7°$, and (d) $\alpha = 15{\cdot}5°$; $M_\infty = 0{\cdot}3$, $Re = 2{\cdot}7 \times 10^6$, turbulent. - - -, boundary layer solution (Jang *et al.* 1991); ——, present zonal solution.

view of the computed density field. The location of the zonal boundary is shown in this figure, and the density contours cross this boundary without distortion. The computed Mach contours at $\alpha = 15{\cdot}5°$ are shown in Figure 9(b). A detail of the leading edge region in Figure 9(c) shows that for a subsonic speed of $M_\infty = 0{\cdot}3$ a significantly high local Mach number, $M = 1{\cdot}3$, is reached at the leading edge. The computed results, however, do not indicate any shock formation. The unsteady solution for the ramp motion was obtained without TVD limiting.

6.2. Oscillatory Motion

The unsteady solution for an oscillatory motion at $M_\infty = 0{\cdot}6$, $Re_c = 4{\cdot}8 \times 10^6$, in a range given by $\alpha(t) = 4{\cdot}86 + 2{\cdot}44 \sin(\omega t)$ with a reduced frequency $k = 0{\cdot}16$ was also obtained. Here the reduced frequency is defined as $k = \omega c / U_\infty$. The flow for this motion is initially purely subsonic; but, as the angle of attack increases to about $\alpha(t) \approx 5°$, supersonic flow conditions are encountered at the leading edge region and a transonic shock forms. This shock is present during the upstroke until the maximum angle of attack is reached and during the downstroke to about $\alpha(t) \approx 5{\cdot}0°$. The

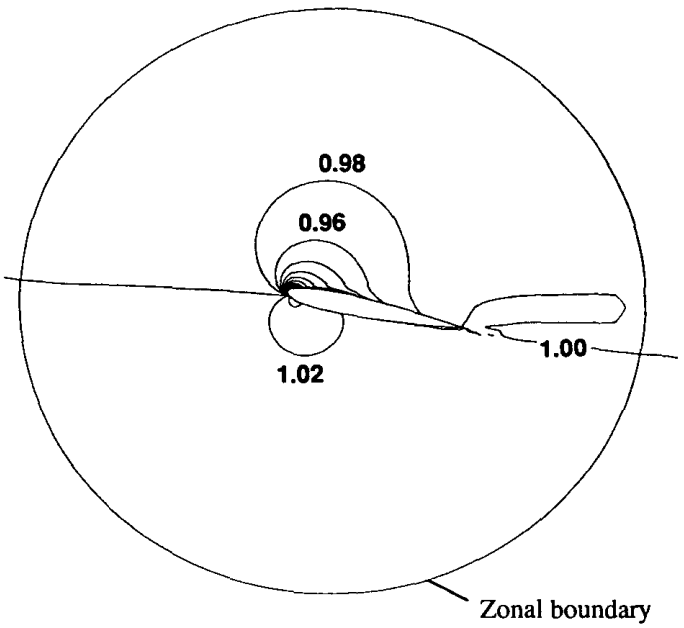

(a)

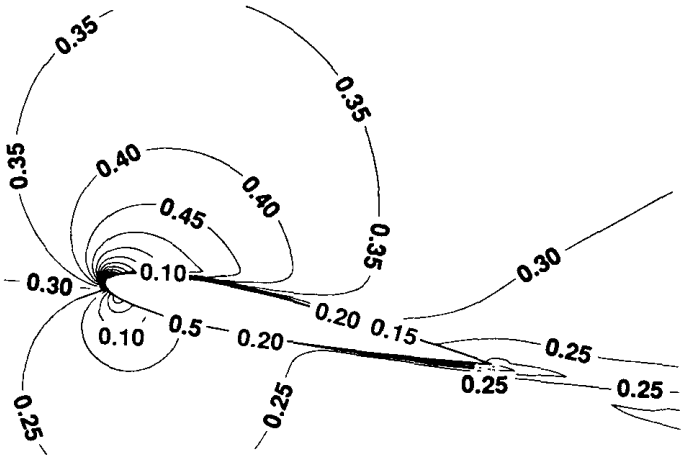

(b)

Figure 9. Computed unsteady flow field at $\alpha = 15{\cdot}5°$; $M_\infty = 0{\cdot}3$, $Re = 2{\cdot}7 \times 10^6$, turbulent. (a) Global view; (b) close-up to airfoil; (c) detail of leading edge region.

computed and measured lift and pitching moment response are compared in Figures 10(a) and 10(b), respectively. The computed lift and pitching moment coefficients are in close agreement with the measured values.

The computed surface-pressure distribution is compared with the measurements by Landon (1982) for two angles during the upstroke and two angles during the downstroke in Figure 11(a–d). The computed surface pressure is in better agreement with the measurements at the lower angles of incidence ($\alpha = 5{\cdot}95°$ up and $\alpha = 5{\cdot}11°$ down). At higher incidences [Figure 11(b, c)], the agreement deteriorates in the region around the shock. The computed flowfield at the higher angles of incidence, $\alpha = 6{\cdot}97°$ up, showed a small separated flow region after the shock.

The computed flow field at $\alpha = 6{\cdot}97°$ during the upstroke is shown in Figure 12(a–c). The global view of the computed density field of Figure 12(a) shows that the density contours smoothly cross the zonal interface for the case where a shock exists. The

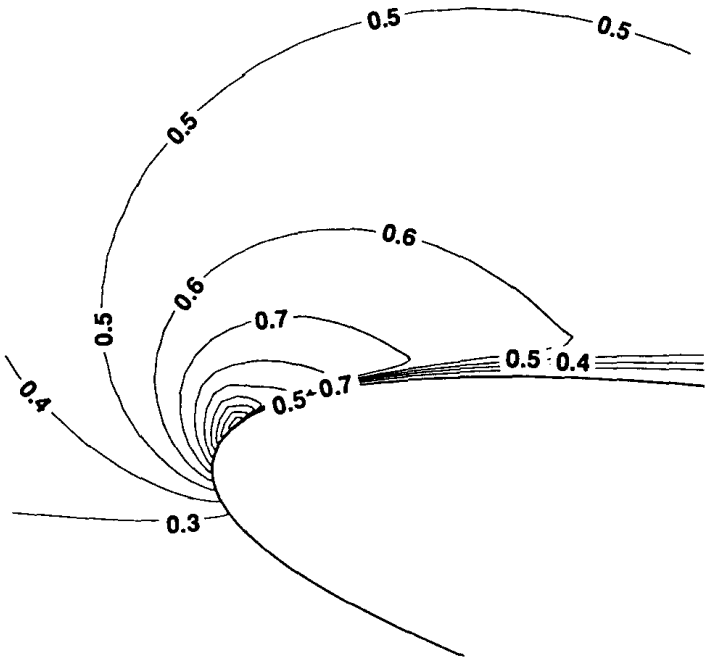

(c)

Figure 9—(*contd.*)

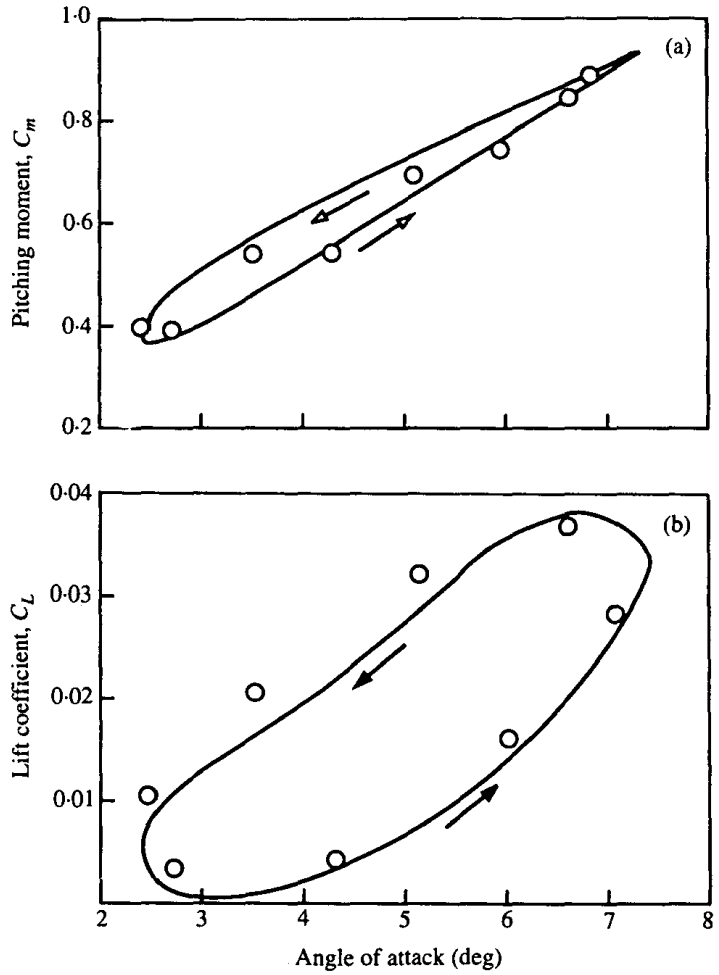

Figure 10. Comparison of the measured and computed (a) lift and (b) pitching moment coefficient for oscillatory motion $\alpha(t) = 4{\cdot}86 + 2{\cdot}44\sin(\omega t)$ with $k = 0{\cdot}16$; $M_\infty = 0{\cdot}60$, $Re = 4{\cdot}8 \times 10^6$, turbulent. ○, Measured (Landon 1982); ——, computed (181 × 56 grid).

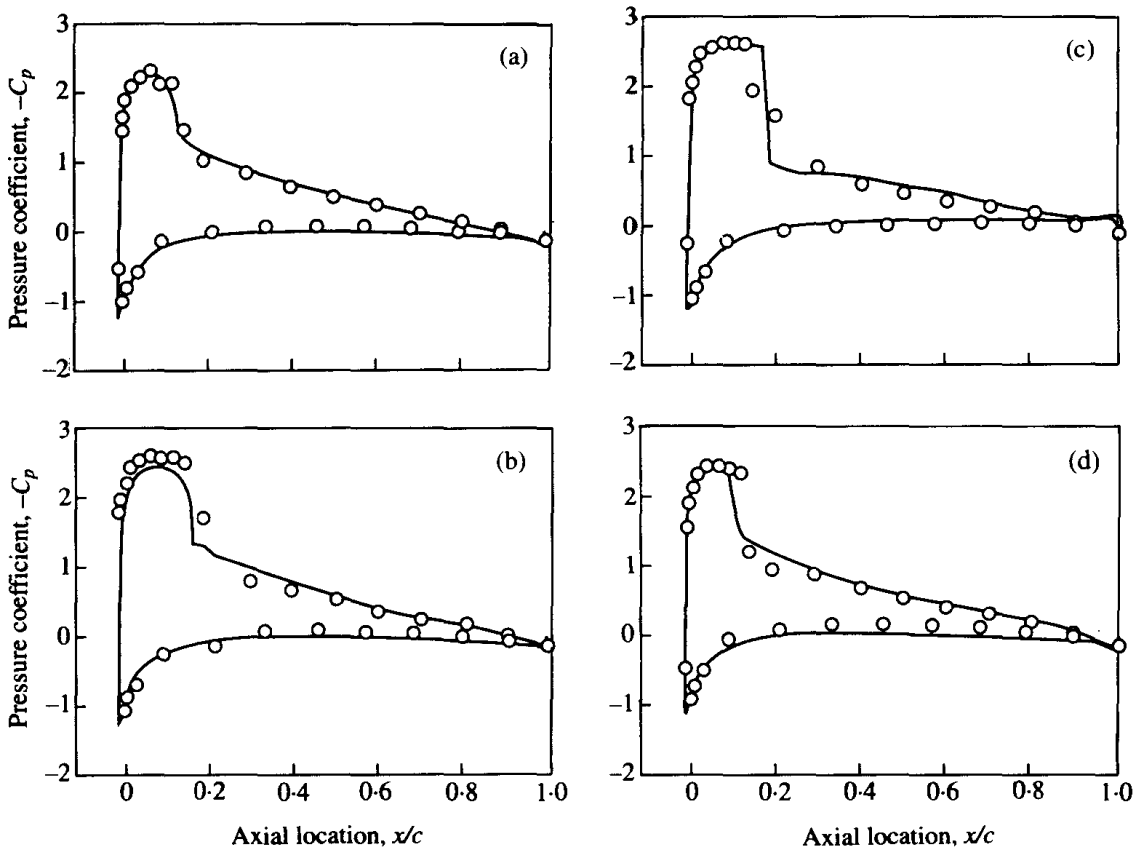

Figure 11. Comparison of the measured and computed unsteady surface-pressure coefficient for oscillatory motion $\alpha(t) = 4{\cdot}86 + 2{\cdot}44\sin(\omega t)$ with $k = 0{\cdot}16$; $M_\infty = 0{\cdot}6$, $Re = 4{\cdot}8 \times 10^6$, turbulent. (a) $\alpha = 5{\cdot}95°$; up; (b) $\alpha = 6{\cdot}97°$, up; (c) $\alpha = 6{\cdot}57°$, down; (d) $\alpha = 5{\cdot}11°$, down.

close-up of the computed density field at $\alpha = 6{\cdot}97°$ shows the shock location. The shock location is also indicated with the Mach contours in Figure 12(c). The entire unsteady solution for the oscillatory motion was obtained using the flux limiters.

7. CONCLUSIONS

A solution procedure suitable for steady and unsteady compressible flow solutions on zonal grids was developed. An implicit upwind scheme was used for the numerical solution. Simple weighted averaging was used at the overlapped zonal interfaces. This approach enables a more economical, flexible, and accurate computation of the flowfield, as compared to a standard Navier–Stokes solver, because the solution of the outer inviscid region is computed on a sparser grid with a computationally less demanding Euler solution, while the near wall viscous region is computed on a finer grid. The present zonal approach yields a 30% reduction in computational time as compared to a full Navier–Stokes solution, without compromising the accuracy of the solution. In addition, the outer boundaries of the stationary, inviscid grid may conform to a specified shape, while the inner grid is moving. Steady, inviscid and viscous flow solutions for subsonic and transonic flows over airfoils were presented to validate the zonal grid approach. Viscous solutions for unsteady transonic and subsonic flows showed good agreement with experimental measurements.

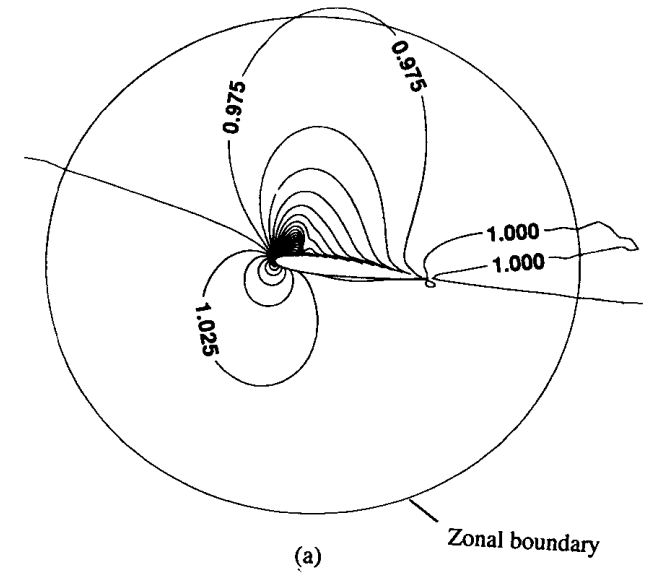

(a)

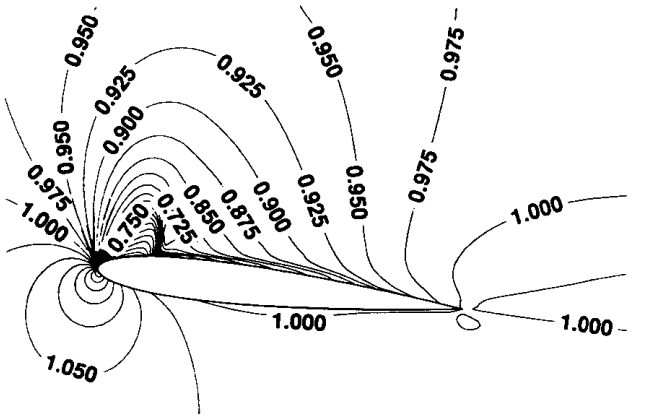

(b)

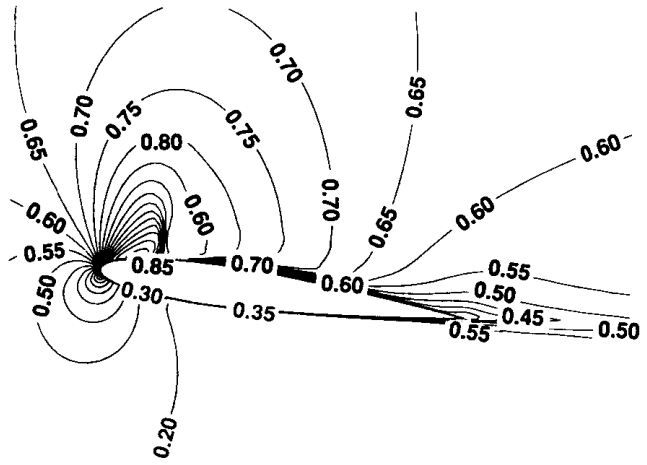

(c)

Figure 12. Computed unsteady flow field; $\alpha = 6{\cdot}97°$ $M_\infty = 0{\cdot}60$, $Re = 4{\cdot}8 \times 10^6$, turbulent. (a) Global view; (b) close-up view; (c) Mach contours.

References

Baldwin, B. S. & Lomax, H. 1978 Thin layer approximation and algebraic model for separated turbulent flows. AIAA Paper 78–257.

Benek, J. A., Bunning, P. G. & Steger, J. L. 1985 A 3D Chimera grid embedding technique. AIAA Paper 85–1523.

Chakravarthy, S. R. & Osher, S. 1985 A new class of high accuracy TVD schemes for hyperbolic conservation laws. AIAA Paper 85-0363.

Chandrasekhara, M., Ahmed, S. & Carr, L. 1990 Schlieren studies of compressibility effects on dynamic stall of airfoils in transient pitching motion. AIAA Paper-90-3038.

Chesshire, G. & Henshaw, W. D. 1990 Composite overlapping meshes for solution of partial differential equations. *Journal of Computational Physics* **90,** 1–64.

Clarkson, J. D., Ekaterinaris, J. A. & Platzer, M. F. 1993 Computational investigation of airfoil stall flutter. In *Unsteady Aerodynamics, Aeroacoustics and Aeroelasticity of Turbomachines and Propellers* (ed. H. M. Atassi), pp. 415–432. Springer-Verlag.

Ekaterinaris, J. A. 1089 Compressible Studies on Dynamic Stall. AIAA Paper 89-0024.

Harris, C. D. 1981 Two-dimensional aerodynamic characteristics of the NACA 0012 airfoil in the Langley 8 foot transonic pressure tunnel. NASA TM 81927.

Hirsch, C. 1990 *Numerical Computation of Internal and External Flows* New York: Wiley.

Hänel, D. 1992 Computational techniques for solving the Navier–Stokes equations. AGARD-CP-510, Paper No. 1.

Jang, H. M., Ekaterinaris, J. A., Platzer, M. F., & Cebeci, T. 1991 Essential ingredients for the computation of steady and unsteady boundary layers. *Journal of Turbomachinery* **13,** 608–616.

Johnson, D. A. & King, L. S. 1985 A mathematically simple turbulence closure model for attached and separated turbulent boundary layers. *AIAA Journal* **23,** 1864–1692.

Landon, R. H. 1982 NACA 0012 Oscillatory and transient pitching. AGARD-R-702.

Osher, S. & Solomon, F. 1982 Upwind difference schemes for hyperbolic systems of conservation laws. *Mathematics of Computation* **38,** 339–374.

Osher, S. & Chakravarthy, S. R. 1983 Upwind schemes and boundary conditions with applications to Euler equations in general geometries *Journal of Computational Physics* **50,** 447–481.

Rai, M. M. 1986 A relaxation approach to patched-grid calculations with the Euler equations. *Journal of Computational Physics* **66,** 99–131.

Rai, M. M. 1987a Navier–Stokes simulations of rotor-stator interaction using patched and overlaid grids. *AIAA Journal of Propulsion and Power* **3,** 387–396.

Rai, M. M. 1987b Unsteady three-dimensional Navier–Stokes simulations of turbine rotor-stator interaction. AIAA Paper 87-2085.

Rai, M. M. & Chakravarthy, S. R. 1986 An implicit form of the Osher upwind scheme. *AIAA Journal* **24,** 735–743.

Roe, P. 1985 Some contributions to the modeling of discontinuous flows. Large Scale Computations in Fluid Mechanics. *Lectures in Applied Mathematics, American Mathematical Society,* Vol. 22, pp. 161–193.

Rumsey, C. L. & Anderson, W. K. 1988 Some numerical and physical aspects of unsteady Navier–Stokes computations over airfoils using dynamic meshes. AIAA Paper 88-0329.

Steger, J. L. & Warming, R. F. 1981 Flux vector splitting of the inviscid gas dynamic equations with applications to finite-difference methods. *Journal of Computational Physics* **40,** 263–293.

Visbal, M. R. 1988 Effect of compressibility on dynamic stall of a pitching airfoil. AIAA Paper 88-0132.

Yakhot, V., Orszag, S. A. 1986 Renormalization group analysis of turbulence. I. Basic theory. *Journal of Scientific Computing* **1,** 1–31.

Yee, H. C., Warming, R. F. & Harden, A. 1983 Implicit total variation diminishing (TVD) schemes for steady-state calculations. NASA TM-84323.

Yee, H. C., 1989 A class of high-resolution explicit and implicit shock-capturing methods. NASA-TM 101088.